Chanyoung Park
Department of Mechanical and Aerospace Engineering,
University of Florida,
Gainesville, FL 32611
e-mail: cy.park@ufl.edu

Justin Matthew
Department of Mechanical and Aerospace Engineering,
University of Florida,
Gainesville, FL 32611
e-mail: jtmathew@live.com

Nam H. Kim[1]
Mem. ASME
Department of Mechanical and Aerospace Engineering,
University of Florida,
Gainesville, FL 32611
e-mail: nkim@ufl.edu

Raphael T. Haftka
Department of Mechanical and Aerospace Engineering,
University of Florida,
Gainesville, FL 32611
e-mail: haftka@ufl.edu

Epistemic Uncertainty Stemming From Measurement Processing—A Case Study of Multiphase Shock Tube Experiments

Experiments of a shock hitting a curtain of particles were conducted at the multiphase shock tube facility at Sandia National Laboratories. These are studied in this paper for quantifying the epistemic uncertainty in the experimental measurements due to processing via measurement models. Schlieren and X-ray imaging techniques were used to obtain the measurements that characterize the particle curtain with particle volume fraction and curtain edge locations. The epistemic uncertainties in the experimental setup and image processing methods were identified and measured. The effects of these uncertainties on the uncertainty in the extracted experimental measurements were quantified. The influence of the epistemic uncertainty was significantly higher than the experimental variability that has been previously considered as the most important uncertainty of experiments. [DOI: 10.1115/1.4042814]

1 Introduction

The validation of scientific computational models has traditionally been done by comparing model predictions against experimental measurements [1–3]. Uncertainty quantification has been the key ingredient in the modern validation process, where the distribution of model predictions is compared with that of experimental measurements [4,5]. Nominally identical experiments are repeated multiple times in order to quantify uncertainty from various sources. During the experiments, the uncertainty in the input parameters/conditions as well as that of the quantities of interest (QoIs) are measured. Then, the uncertainties in the input parameters/conditions are propagated through the physical model to produce the distribution of predictions. The validation is conducted using various validation metrics based on the two distributions [6,7].

Often experimental variability has been considered as a major uncertainty source. However, epistemic uncertainty in measurement process also has received attention. Ferson et al. [8] address the needs of the characterization of measurements including epistemic uncertainty and suggest an interval estimation instead of point estimation. Beresh [9] suggests detailed comparisons of data sets from redundant measurement methods that introduce different epistemic uncertainties for the same experiment to capture the error source of experiment. Hughes et al. [10] demonstrate the importance of experiment configuration design for minimizing epistemic uncertainty in measurement process based on legacy data and past documentation. Thurber [11] discusses the influence of various characteristics of acetone on planar laser-induced fluorescence imaging and is to make diagnostics quantitative. Adrian and Westerweel [12] discuss various aspects of particle image velocimetry image processing including theoretical models and possible error sources. Timmins et al. [13] suggest a method to obtain measurement uncertainty from the epistemic uncertainty in parameters for the particle image velocimetry algorithm to process experimental data. Hughes et al. [14] introduce the concept of forensic uncertainty quantification (UQ) for simulation validation. Forensic UQ proposes an independent investigator to discover possible missing uncertainty sources in validation-quality experiments. The concept is demonstrated with an explosion experiment performed at the Eglin Air Force Base. The epistemic uncertainty in the model prediction comes from model error, numerical error, and/or discretization error. When the two distributions fail to match, it is often concluded that the model is invalidated. The objective of this paper is to show that there can be a significant portion of epistemic uncertainty in experiments too. Sometimes, this epistemic uncertainty may be larger than the aleatory uncertainty. In such a case, it is required to have a careful assessment of uncertainties in order to obtain a meaningful outcome from the validation. The objective of this paper is to demonstrate the potential significance of epistemic uncertainty in experiments using the case study of the multiphase shock tube experiments that were conducted by Sandia National Laboratories [15–18].

The major source of epistemic uncertainty in experiments occurs when the QoI is measured indirectly. While attempting to measure the QoI, the experimentalist typically measures an intermediate quantity that allows obtaining the QoI. The process of converting the intermediate quantity into the QoI often involves a model or assumptions. For example, a strain gage may be used to measure the strain in a beam, but it actually measures the change in voltage. A linear model between the change in voltage and strain is used to calculate the strain. Therefore, the uncertainty in measured voltage is propagated through the model to yield the uncertainty in strain. However, as the complexity of such models increases, the propagation of uncertainty becomes less trivial, and it becomes a major source of epistemic uncertainty.

In the present paper, we illustrate the importance of quantifying epistemic uncertainty in QoI using a series of shock-particle

[1]Corresponding author.
Manuscript received June 18, 2018; final manuscript received February 4, 2019; published online March 7, 2019. Assoc. Editor: Scott Doebling.

interaction experiments run on the multiphase shock tube at Sandia National Laboratories. The study was motivated by the development of a shock-particle curtain interaction simulation and the necessity for validating the simulation program [15,19,20]. Experimental measurements were to be compared with simulation results to assess the validity of the simulation. The challenge in this case is the indirect nature of critical experimental measurements, the particle volume fraction, and the location of the curtain, which are obtained from X-ray and Schlieren image that require two separate postprocessing models. X-ray and Schlieren images have pros and cons. They are, respectively, used to measure curtain volume fraction at $t = 0$ and particle front position at different time exclusively. Wagner et al. [21] discuss that it is not possible to measure volume fraction using Schlieren images since the particle curtain is completely opaque towards visible light.

The experiments involve a planar shock wave impinging on a particle curtain formed inside the rectangular frame of the shock tube (shown in Fig. 1). The shock wave is generated by a high-pressure ratio between the driver and driven sections when a diaphragm between them is burst. The particle curtain is formed when the particles in the reservoir fall down through a narrow slit. When the shock hits the particle curtain, it makes the particle curtain expand and move downstream. Schlieren and X-ray imaging techniques are used to capture the motion of the particle curtain and to measure the distribution of the volume fraction from the images [22]. The data extraction process involves complicated calculations. These calculations are derived from physical models that define the relationship between the QoI and the images as well as calibrating model parameters from other experiments. Therefore, the measurement process includes epistemic uncertainty. As the models become more complicated, they will likely contribute a significant amount of epistemic uncertainty in the calculations of the desired measurements.

Our studies associated with the particle curtain characterization revealed important sources of epistemic uncertainty that significantly increased the overall uncertainty in the QoI. Traditionally, model form errors in simulation are considered as the dominant sources of epistemic uncertainty in validation exercises. However, we emphasize that complex measurement processing in experiments may act as major uncertainty sources that should be thoroughly considered.

The paper is organized as follows: Sec. 2 explains details of the experimental setup and the measurement process for Schlieren and X-ray. Section 3 describes the process of uncertainty quantification for these processes. Section 4 shows the comparison between the aleatory and the epistemic uncertainty, followed by conclusions in Sec. 5.

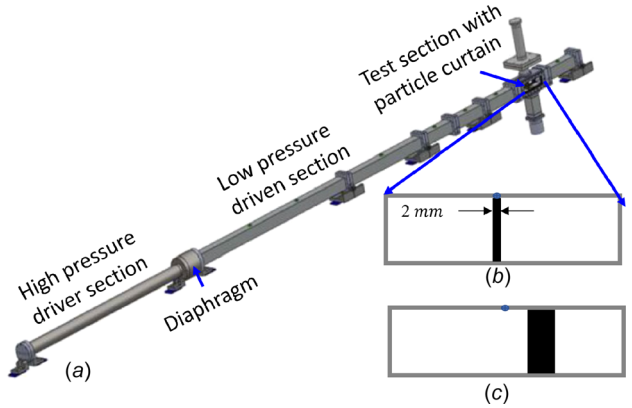

Fig. 1 Schematic figure of the shock tube experiment: (*a*) Sandia multiphase shock tube, (*b*) particle curtain before impact, and (*c*) particle curtain after impact

2 Shock-Tube Imaging Experiments

The shock tube experiments were initially conducted at the multiphase shock tube in Sandia National Laboratories [16]. The shock tube apparatus consists of two sections separated by a diaphragm: a high-pressure driver section and a low-pressure driven section. Once the diaphragm bursts, a shock wave is generated due to pressure difference, and it propagates toward the test section as shown in Fig. 1(*a*). Although the original experiments were conducted for various shock speeds, we only analyze the case of Mach 1.67 in this paper. The particle curtain is formed by falling particles, under the influence of gravity, through a 3.2 mm beveled slit in the particle reservoir, forming about 2 mm thick curtain in the test section. Soda-lime particles with the average diameter of 115 μm are used for the experiment. Figure 1(*b*) shows a schematic side view of the initial particle curtain. Once the shock wave reaches the particle curtain from the left, the curtain expands and moves to the downstream, where the downstream edge moves faster than the upstream edge, as shown in Fig. 1(*c*).

Measurements of the experiment are conducted via two imaging systems: Schlieren and X-ray radiography. Both systems are aimed at the window in the test section shown in Fig. 1, where the motion of the particles can be visible. Note that each experiment is recorded with Schlieren or X-ray images, not both, because they cannot share the observation window of the test section.

Two QoIs are required for simulation validation. The first is the position of upstream and downstream particle curtain fronts, which track the expansion and movement of the particle curtain fronts as a function of time. The curtain thickness is obtained as the difference between the two front positions. Experimentally, the particle front positions are obtained from high-speed Schlieren imaging system, which will be compared with the simulation predictions to assess the validity of the simulation. The second QoI is the distribution of particle volume fraction within the curtain, which can be measured using the flash radiography (X-ray) technique. A unique aspect of these QoIs is that they can be used for both the input to the simulation and the QoI for validation. Before the shock hits the curtain, these two QoIs can be used as the initial condition of the simulation, while after the shock hits the curtain, they will be used as the QoI for validation.

The postprocessing of the raw data is largely done through physics-based image analysis techniques. Figure 2 depicts the process of obtaining the particle volume fraction and the locations of particle curtain fronts. The images of the particle curtain are obtained with a high-speed Schlieren imaging system to capture the motion and expansion of the curtain as the shock impinges on the curtain. X-ray images are used to measure particle volume fraction. This process is supported by the X-ray calibration experiment that calibrates the attenuation of the X-rays due to the particle volume that they pass through. This experiment calibrates the X-ray image processing. The introduction of the calibration experiment brings an additional source of uncertainty in measurement processing.

As shown in Fig. 2, the three experiments produce input parameters for the simulations as well as output QoIs for validating the simulations. The input parameters are those experimental measurements that define the initial conditions of the simulations. Experimental measurements at time $t = 0$ or before the shock hits the curtain yield information about these input parameters. These include the initial curtain thickness and the initial distribution of particle volume fraction both obtained from the Schlieren and X-ray images of the curtain before shock impingement, respectively. On the other hand, the experiments also measure the output QoIs that are used to validate simulation predictions. The primary validation QoI is the particle curtain front locations over time measured via the Schlieren experiments. The secondary validation QoI is the distribution of particle volume fraction over time measured by the X-ray experiments. Additionally, the X-ray experiments require X-ray parameters that are obtained from X-ray calibration experiments. These parameters are used in X-ray experiments to

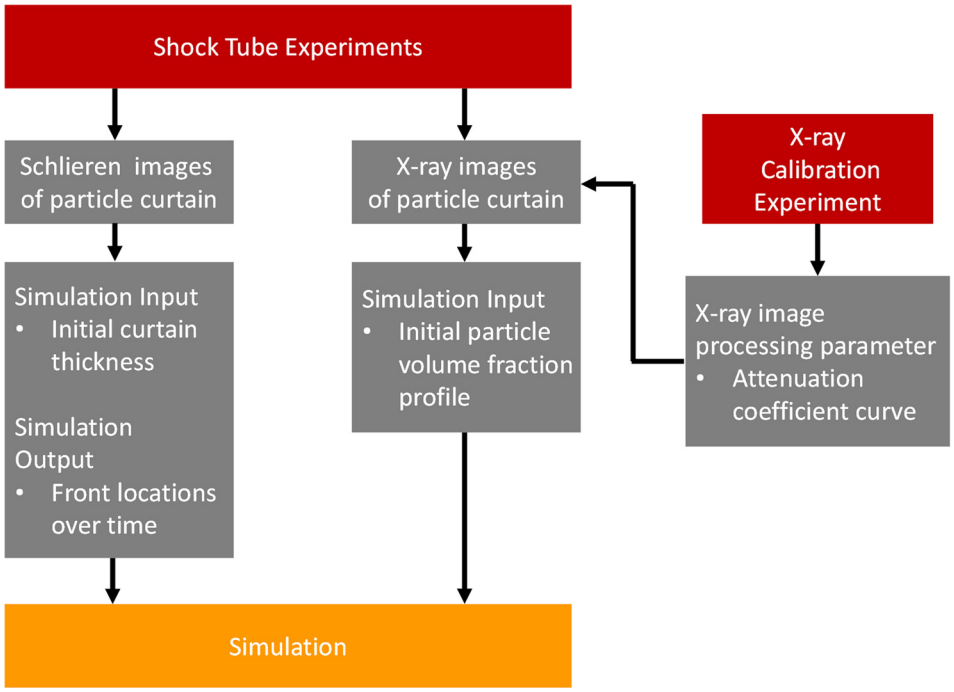

Fig. 2 Experimental postprocessing procedure

estimate the particle volume fraction from X-ray image intensity. The approximation process in these X-ray parameters contributes to the epistemic uncertainty in the measurement process.

2.1 Schlieren Measurement Processing. The Schlieren imaging system measures the front locations over time, which are used as the primary validation QoI for simulations. The images produced by the experiment must undergo postprocessing in order to find the particle curtain locations. The postprocessing is an inverse process based on the physics of light that explains how a particle curtain appears on the Schlieren image [16].

2.1.1 Schlieren Imaging. Schlieren photography is a technique used to visualize density variations in a fluid flow. These variations or gradients of density cause the deflection of light. When the light meets a region with a high gradient of density, the light is deflected toward or away from the region, which produces a shadow pattern. This shadow pattern is shown as an image intensity depending on the fluid expansion or compression. The technique helps visualize shocks and other flow characteristics, and for the purpose of identifying particle curtain fronts, it is straightforward, as the solid particles show up in strong shadow. The density variation between a particle and the air around it simplifies the Schlieren imaging process. Figure 3 shows particles captured on a Schlieren image with consistent contrast against the background. The major advantage of Schlieren photography is that it can capture both the shock location and the particle curtain locations.

2.1.2 Image Processing. Using the Schlieren images obtained from Wagner et al. [21], the postprocessing for determining the particle curtain fronts was performed with uncertainty quantification. The Schlieren photography produced approximately 20 images showing the expansion of the curtain after the shock hits the curtain. Figure 3 depicts some of these images where Fig. 3(*a*) shows the curtain before the impingement of the shock (the shock is located to the left of the curtain), while Fig. 3(*b*) shows the expansion of the particle curtain after the shock passes through it. The bowed particle curtain in the *y*-direction is due to boundary effects. It is reasonable to expect smaller boundary effects to occur near the sidewalls where there is a small air gap between the curtain and the wall. The particle curtain forming apparatus on top of the test section blocks the view of the curtain in the *z*-direction. Although the Schlieren images shown in Fig. 3 capture almost the entire portion of the curtain, the center portion within the two white lines with a height of 5 mm is used for analysis to avoid the effects of varying curtain thickness in the vertical direction and boundary effects near the top and bottom. Quantifying the uncertainty due to boundary effects is not feasible but the uncertainty is considered little based on expert opinion. In order

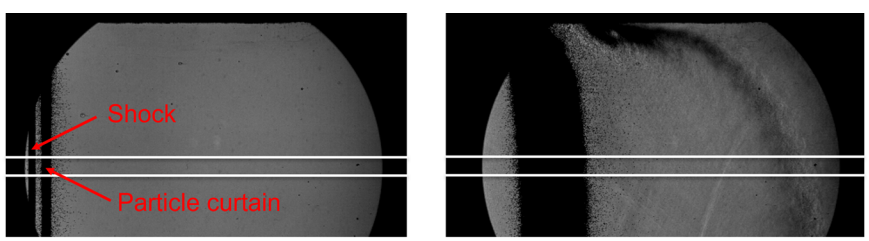

(*a*) (*b*)

Fig. 3 Schlieren image of curtain: (*a*) particle curtain before impact and (*b*) particle curtain after impact

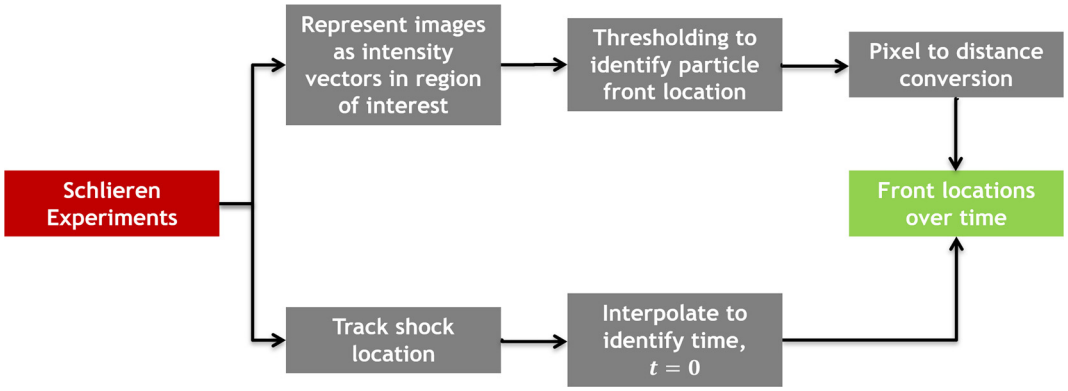

Fig. 4 Schlieren measurement processing

to minimize the boundary effect, the particle front locations are calculated based on the middle section of the images. This also helps expand the field of view. The effect of gravity can be ignored because the time span of the shock-curtain interaction captured in this experiment is a several orders of magnitude less than that of the gravity. The curtain fronts are then identified using a threshold of image intensity for different time frames.

Figure 4 depicts the image processing conducted to obtain the particle front locations. First, the image is cropped to the region of interest, which is the region between the white lines in Fig. 3. Next, the average pixel intensity was calculated across the pixels at the same horizontal location to produce an averaged intensity vector representing every location in the horizontal direction. Then, the front location is obtained on either side of the curtain by finding the pixel location where the averaged intensity is closest to the 5% of the average background intensity. The last step is to calculate the curtain thickness by multiplying the number of pixels with the size of one pixel.

Another important aspect of the image processing is how to identify the initial time. Time, $t = 0$, is defined as the moment when the shock first encounters the curtain. In fact, simulation will position the shock at the left curtain front location when $t = 0$.

2.2 X-Ray Measurement Processing. The X-ray experiments have higher measurement processing complexity for obtaining initial volume fraction. Thus, the uncertainties in the process need rigorous quantification. As depicted in Fig. 2, the X-ray image processing requires a separate calibration experiment to convert the image intensity to the volume fraction. Since Schlieren imaging alone is unable to obtain a volume fraction measurement, Wagner et al. [17,21] switched the imaging apparatus to an X-ray method, which was expected to reduce the uncertainty.

2.2.1 X-Ray Measurement Setup. The X-ray imaging technique was setup to measure the variations of particle volume fraction along the streamwise direction by measuring X-ray beam intensity reduction. Wagner et al. [21] note that the X-ray images are obtained with a computer radiograph system that is composed of a Carestream Industrex digital imaging plate having a spatial resolution of 100 microns and an ALLPRO Imaging scanner (ALLPRO Imaging, Melville, NY). Since Schlieren imaging could not penetrate the opaque curtain, a top-hat volume fraction distribution was assumed, resulting in a large uncertainty in the volume fraction. The X-ray technique described in Ref. [21] employed the X-ray setup shown in Fig. 5.

The stationary X-ray source was aligned accurately with the particle curtain. To avoid the error due to misalignment, X-ray was used not to measure the particle front positions but to measure the volume fraction at $t = 0$. The uncertainty due to misalignment is considered little in the paper.

The X-ray experimental data are limited to one image per experiment because of the inability of an X-ray apparatus to flash rapidly. After one exposure, the X-ray source must be recharged. Thus, five time-points, $t = 0$, 110, 180, 230, and 340 μs, were selected and four repetitions were conducted at each time point resulting in 20 total experiments. The X-ray source is positioned to align with the center of the curtain at a given time for each of the experiments in order to minimize the error due to misalignment. In addition, since the distance between the X-ray source and the particle curtain was much larger than the movement of the curtain for the times of flashing, the effect of misalignment is expected to be little. In Sec. 3, it will be shown that this misalignment can cause an error in measuring the distribution of volume fraction, which will be considered as epistemic uncertainty.

2.2.2 X-Ray Image Processing. Figure 6 shows the X-ray images of the test section. The X-ray images are cropped to an approximately 20 mm vertical section outlined in Fig. 6(*b*) with white lines, and the image intensities are averaged over the vertical direction to create an average intensity for every location along the streamwise direction. The intensities are used to estimate the volume fraction by following the formulation from Wagner et al. [21].

The method used to convert intensity to volume fraction is based on the assumption that the volume fraction is proportional function to the intensity ratio. Since X-ray beam intensity decays while passing through the soda-lime particles, the ratio between the X-ray intensities of the curtain and background tells the traveling distance, w, of the X-ray beam through the particles. When the width of the particle curtain is w_0, the volume fraction φ_p can be estimated as

$$\varphi_p = \frac{w}{w_0} \tag{1}$$

where w is the path length the X-ray beam through particles (the rest of the path is through air with negligible attenuation). Although the shape of particles is spherical, since we average the intensity over the vertical direction, Eq. (1) will be a good approximation of the volume fraction.

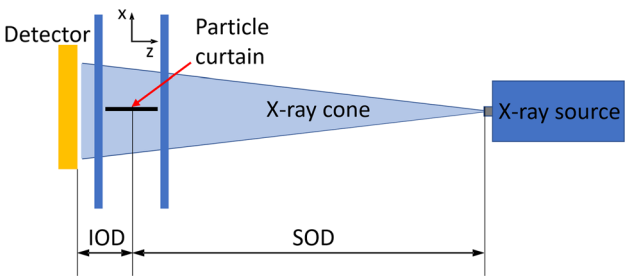

Fig. 5 Multiphase shock tube X-ray apparatus schematic

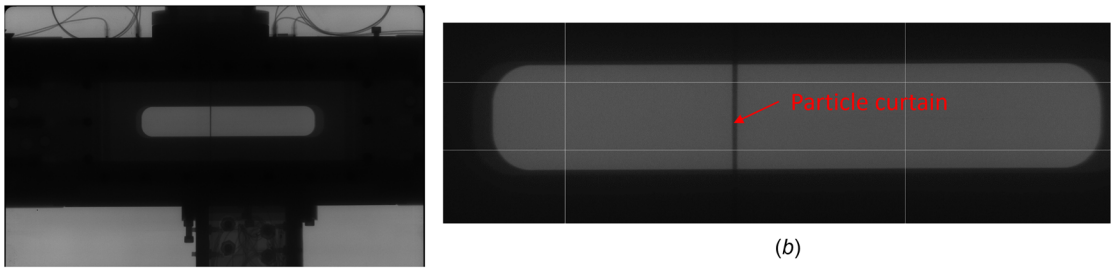

(*a*) (*b*)

Fig. 6 X-ray image of the particle curtain: (*a*) raw X-ray image of test section and (*b*) particle curtain X-ray image

The Beer–Lambert law [23] calculates the attenuated intensity I of X-rays after traveling through a medium with density ρ and thickness w when the intensity without the medium is I_0. The relationship is given as

$$I = I_0 e^{-A\rho w} \tag{2}$$

where A is the X-ray attenuation coefficient.

Wagner et al. [21] used these two relations to create a working form of the Beer–Lambert law to estimate the volume fraction from intensity measurements as

$$\varphi_p = \frac{\ln(I/I_0)}{-A\rho w_0} \tag{3}$$

where I/I_0 represents the ratio between the intensity at the point of interest and the background intensity I_0 from an X-ray image. In the equation, the density of particles is represented by ρ. The value w_0 represents the depth of the particle curtain along the z-axis in Fig. 5.

Since the X-ray is from a point source as shown in Fig. 5, the projected image of the particle curtain is larger than the actual curtain size. Therefore, it is necessary to compensate for the magnification effect before converting X-ray image intensity to the volume fraction profile. Based on the geometries of the experimental setup shown in Fig. 5, the amount of magnification can be calculated using

$$M = \frac{\text{SOD} + \text{IOD}}{\text{SOD}} \tag{4}$$

where image-to-object (IOD) and source-to-object (SOD) are 8 cm and 136 cm, respectively.

As can be seen in Eq. (3), the conversion from image intensity ratio to the volume fraction depends on the attenuation coefficient A. Wagner et al. [21] noted that the attenuation coefficient A is not a constant but a function of the intensity ratio due to the beam hardening effect. In addition, the attenuation coefficient needs to be calibrated. To obtain the functional form of the attenuation coefficient, Wagner et al. [21] conducted a calibration experiment using the glass wedge shown in Fig. 7.

Considering that the height at the center of the glass wedge corresponds to w_0, the volume fraction at the center equals to one. As the height w decreases toward the tip, the volume fraction gradually decreases. X-rays are projected down toward the top of the glass wedge in Fig. 7. Since the height of each step (w) and the density of the material (ρ, the same soda-lime glass material as the particles) are known, and since the intensity ratios for each step are measurable from the X-ray image from the calibration experiment, the attenuation coefficient of each step can be calculated using Eq. (2). Figure 8 shows the attenuation coefficient data (hollow circles) at different steps and a linear fit for the data. Wagner et al. [21] fit the data using a linear function for the attenuation coefficient, which was used to obtain the volume fraction from the X-ray experiments of the curtain. As shown in Fig. 8, the linear fit captures the trend of data but also shows modeling errors. The effect of the modeling error due to this linear assumption will be investigated in Sec. 3.

The image processing workflow of the X-ray experiments is depicted in Fig. 9, where both the calibration and the X-ray curtain experiments contribute to the calculation of the particle volume fraction of the curtain. The top half depicts the calibration

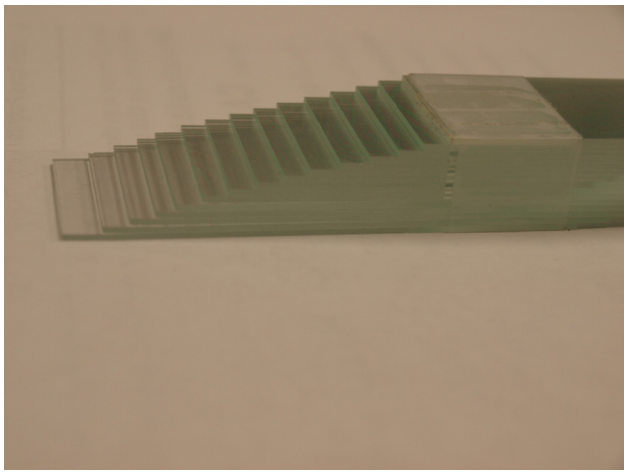

Fig. 7 Glass wedge for X-ray calibration experiment

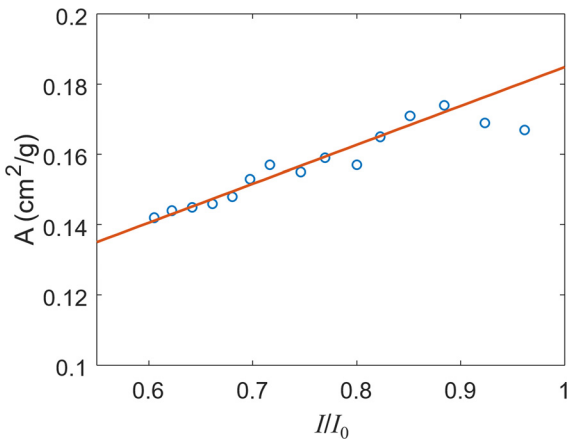

Fig. 8 Calibration experiment results for attenuation coefficient

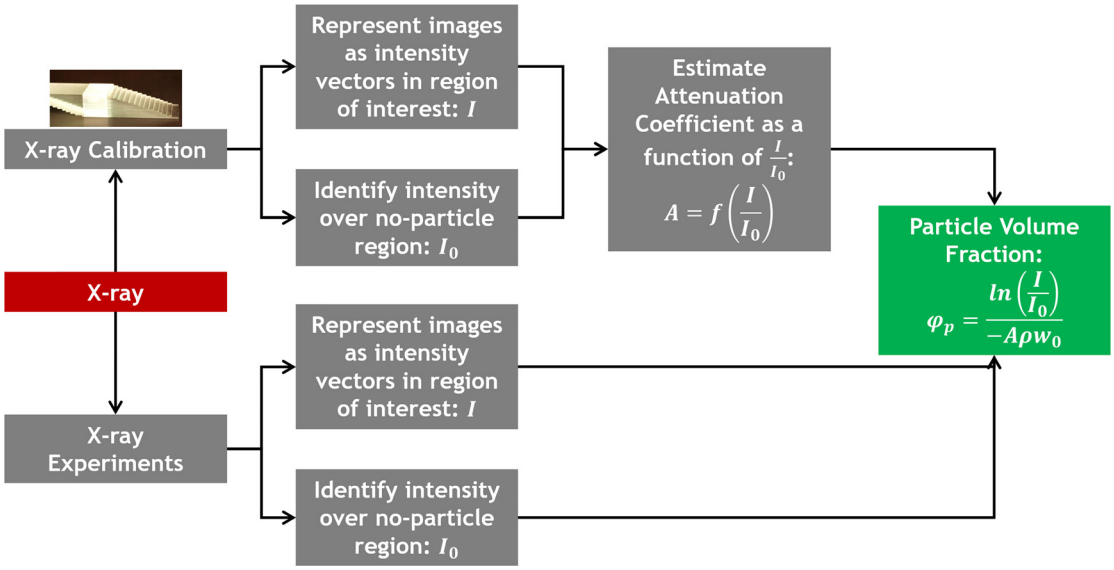

Fig. 9 X-ray measurement processing

experiment described previously, while the bottom half describes the X-ray experiment.

3 Uncertainty Quantification of Measurement Processing

In this section, the uncertainty in the QoIs from the two imaging systems in Sec. 2 is quantified. Studying the image processing methods allows us to identify uncertainty sources of QoIs, the locations of particle curtain fronts, and the volume fraction. Measuring the magnitude of these uncertainties and propagating them through the calibration process allow us to quantify the uncertainty in the QoIs.

3.1 Uncertainty Quantification of Schlieren Measurement Processing. A key step in uncertainty quantification is to measure/estimate all possible sources of uncertainty in the experimental process. Table 1 lists the uncertainty sources in the Schlieren image processing step based on Wagner et al. [16]. Table 1 also lists those parameters whose uncertainties were not measured but their influences were assumed ignorable. For example, the Schlieren apparatus was assumed to be placed in perfect alignment with the curtain to eliminate the magnification effect, although the uncertainty in the alignment was not measured.

The main goal is to quantify the effects of the uncertainty sources listed in Table 1 on the front locations. The image and time resolutions had uncertainties that had negligible bearing on the front location estimated by the measurement processing. An assumption is made that the Schlieren light source is collimated since we have no reason to believe otherwise; therefore, we consider that the effect of magnification is ignorable.

Table 1 Uncertainty sources of Schlieren imaging experiment

Uncertainty sources in the image processing	Value
Image resolution	0.226 ± 0.001 pixels/mm
Frame rate of Schlieren imaging system	24.4 ± 0.01 μs
Intensity threshold to define front location	1–20% of maximum intensity
Parameters without uncertainty information	**Assumed value**
Camera and light source alignment	90 deg (perpendicular to test section)
Magnification	1.0

3.1.1 Initial Curtain Thickness. A critical input parameter from the Schlieren experiments is the initial curtain thickness. This is obtained by images taken before the shock hits the curtain. We use 15 images before the shock hits the curtain to represent approximately 350 μs, which is approximately the length of time we study during the shock-curtain interaction. This gives us an idea of how much the curtain thickness varies naturally over the period as well as a value for the curtain thickness for simulation input. Schlieren image analysis showed a mean curtain thickness of 2.38 mm and a standard deviation of 0.1 mm. The variability remained constant within the 350 μs range.

3.1.2 Schlieren Apparatus Alignment. Misalignment in the light source for taking Schlieren image could magnify the curtain as it appears in the image inflating calculations of curtain thickness. Figure 10 depicts a block curtain where a source of collimated light is illuminating the curtain from a slight (dramatized) angle. This slight misalignment captures the side of the curtain, which would present as inflation to the curtain thickness in the image. A trivial ray tracing exercise revealed that a 1 deg misalignment of the light source could cause up to a 1.2 mm distortion in the front location. This is particularly significant for the initial curtain thickness measurements used as inputs to simulations. The four experiments studied in this paper showed curtain

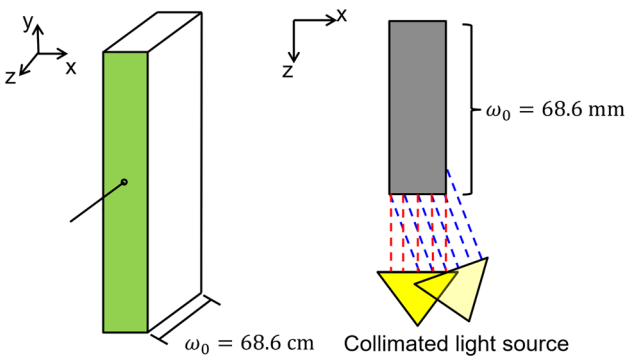

Fig. 10 Schlieren apparatus misalignment

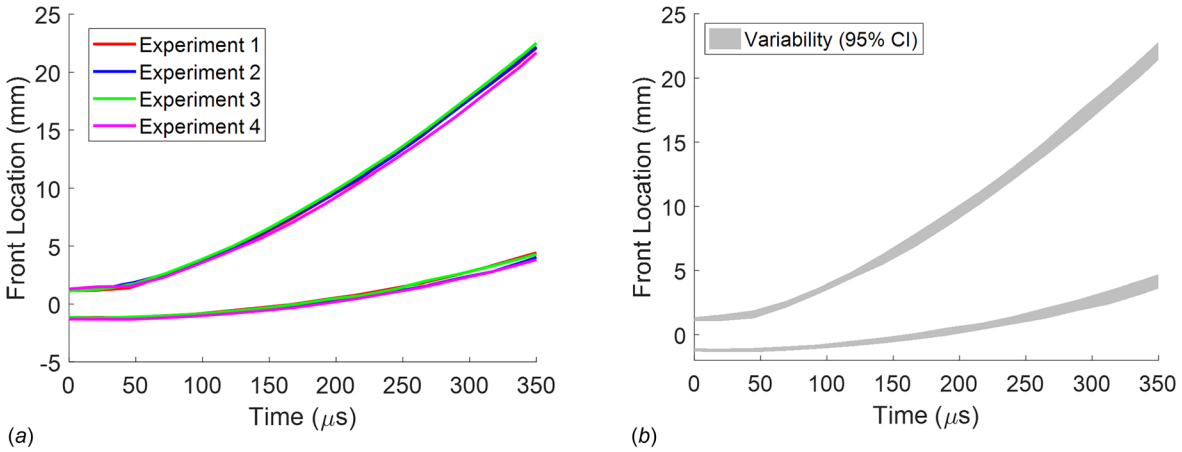

Fig. 11 Schlieren particle front locations: (*a*) front locations (four experiments) and (*b*) averaged front locations with 95% confidence intervals

thickness up to $\delta_0 = 2.38 \pm 0.2$ mm. As described in Table 1, the uncertainty in the misalignment for the shock tube experiments was unavailable. However, later experiments done on the same apparatus by DeMauro et al. [18] measured the particle curtain thickness to be $\delta_0 = 1.5 \pm 0.2$ mm. Therefore, the misalignment should be considered as a significant source of uncertainty in the curtain thickness.

3.1.3 Time Resolution—Identifying $t = 0$. Initial time, $t = 0$ μs, was defined as the moment the shock first hit the left edge of the curtain. Two methods were used to estimate the initial time and the uncertainty. The first method utilized three sequential Schlieren images: one where the shock is seen just upstream of the curve, the second where the shock has passed through the curtain, and a third just after the second. The shock speed is estimated between each pair of images and averaged curtain location (assuming that the shock speed is constant through the curtain). The curtain location at $t = 0$ μs is estimated using the distance between the shock and the curtain in the first image. Estimating $t = 0$ is simply just defining the times associated with each images given the definition of time, $t = 0$ μs. The second method used the average nominal shock speed based on the burst disk and the distance between the shock and curtain in the first image to estimate when the shock hits the curtain. This first image can be seen in Fig. 3(*a*). Uncertainty in the shock speed estimated from the three consecutive images and uncertainty in the average shock speed estimated by the burst disk properties resulted in shock speeds ranging from 2.4 to 2.5 pixels/μs. Then, calculating the adjustment necessary to center the data around $t = 0$ yields an uncertainty of approximately 0.5 μs. That means the particle position has temporal uncertainty of 0.5 μs.

3.1.4 Uncertainty in Threshold. The particle front location is obtained using a threshold. For example, the particle front of the curtain in Fig. 3 is determined by selecting a pixel, whose intensity is lower than the threshold intensity. An ad hoc method is used to select the threshold of 5% to define the front locations in the image analysis [16]. However, it turned out that the variations from 1 to 20% had a negligible effect on identifying the front location (standard deviation of 0.05 mm). It is concluded that the uncertainty due to the threshold selection has a small contribution. This is because of the nature of the particles in the Schlieren images, which present a sharp, consistent contrast against the empty background.

3.1.5 Variability in Experiments. Besides the uncertainties regarding the imaging process, there is variability in experiments. The plot in Fig. 11(*a*) shows the downstream and upstream fronts for four runs. Of note, the fourth run was shifted back a single time interval (24.4 μs) to align with the others because of a suspected processing error. Figure 11(*b*) shows the average of the upstream and downstream fronts over the four experiments. The uncertainty bands represent variability of 95% confidence interval. Since the uncertainty in the time of data is little (0.5 μs), the horizontal error bars of the data are omitted.

3.2 X-Ray Measurement Processing Uncertainty Quantification. Table 2 consists of sources of uncertainty identified in the image processing and the calibration experiment. The average background intensity was measured by averaging intensities from the background pixels of the images without including the particle portion. The uncertainties in the particle density and the curtain width were obtained from the communication with the authors of Wagner et al. [21]. The magnification uncertainty was conservatively estimated by assuming that there is uncertainty in the experiment configuration, using Eq. (4). The uncertainties in the imaging process are little. The largest uncertainty source in terms of coefficient of variation is the uncertainty in the particle density. However, the uncertainty is averaged out in the process of analyzing X-ray images since the process uses integrated density of particles along the beam travel direction. The uncertainty in the location of X-ray source was not measured. The source was precisely placed with a high-load micrometer and it is assumed that its influence on the volume fraction calculation process is little [21,24].

The most important uncertainty in the process is the uncertainty in the attenuation coefficient curve obtained from the calibration experiment. Sections 3.2.1 and 3.2.2 describe the uncertainty quantification of the curve and quantifying the uncertainty in the volume fraction.

3.2.1 Uncertainty Quantification of Attenuation Coefficient Calibration. The attenuation coefficient, A, as discussed before, is estimated as a function of the X-ray image intensity at a point and the background intensity. The calibration experiment with the soda-lime glass block shown in Fig. 7 yielded 15 attenuation coefficients for I/I_0 of the steps. Wagner et al. [21] fit the attenuation coefficient data with a linear function to estimate the volume fraction in the particle curtain experiments. The data, however, have noise and finding the true trend while filtering out the noise and estimating the uncertainty are of key importance. Since the data came from the steps of one block, we assume that the noises are correlated. Since the regular linear regression model assumes independent noise, we developed a linear regression model with correlated noise using a Gaussian process (GP) model in the Appendix.

By applying the developed regression model, a linear fit and the uncertainty in the fit were obtained. Figure 12 shows the 95% confidence interval for the predicted attenuation coefficient curve with a linear model and two randomly generated curves (curves

Table 2 Uncertainty sources regarding X-ray image processing

Uncertainty sources in the image processing	Value
Average background intensity, I_0	20347 ± 8
Particle density, ρ	2.42 ± 0.05 g/cm^3
Curtain width, w_0	68.6 ± 2.0 mm
X-ray image resolution	100 μm (20 cells for 2 mm curtain)
Uncertainty sources in the calibration experiment	**Value**
X-ray source alignment	90 deg (perpendicular to test section) Centered at particle curtain center
Magnification	1.06 ± 0.01

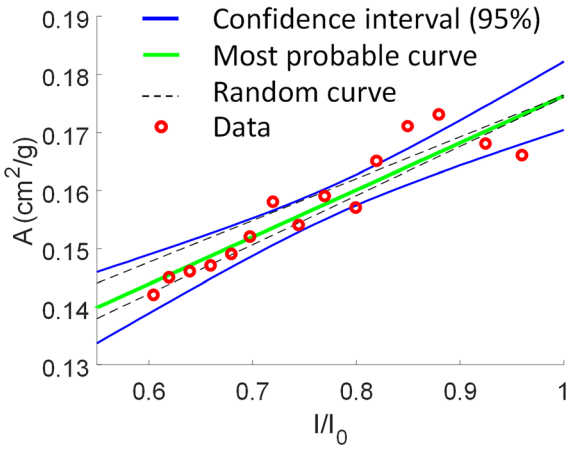

Fig. 12 The 95% confidence interval for the attenuation coefficient curve and two randomly generated curves

with dashed line). The confidence interval represents the uncertainty in the predicted curve. The confidence interval is wider at the sides of the intensity range that represents extrapolation uncertainty. Since the curve is based on the whole noisy data set, the uncertainty in the curve is less than the individual point uncertainty. Note that the uncertainty in the intensity ratio is little because the intensity data were directly obtained from digital images. The horizontal error bars of the data are omitted.

3.2.2 Uncertainty Propagation Through Volume Fraction Calculation Model. The uncertainty in the volume fractions was quantified by propagating uncertainties involved in the process. Thus, the uncertainty in the volume fraction is the result of the attenuation uncertainty, which is due to the data noise and data sparsity causing extrapolation. As discussed, the influence of the uncertainty sources in Table 2 was minimal based on this study, while the uncertainty in the attenuation curve is the dominant uncertainty source. Figure 13(*a*) is the possible attenuation coefficient curves based on the regression model. Figure 13(*b*) shows the quantified uncertainty in the volume fraction calculation at $t = 0$ μs for a single X-ray image.

Note that the model to measure the volume fraction assumes that the attenuation coefficients for spherical particles and the glass calibration plate are identical. However, this assumption may include another model form uncertainty. Thus, it could enlarge the current total uncertainty and it reinforces the importance of measurement uncertainty further.

3.2.3 Variability in Experiments. The plot in Fig. 14(*a*) shows three volume fraction profiles, which are processed based on three experiments. Figure 14(*b*) shows the variability in the volume fraction profiles over the three experiments. The uncertainty bands represent variability of 95% confidence interval obtained from the three profiles in Fig. 14(*a*). Since the X-ray image resolution is high, the spatial uncertainty is ignorable.

Without doubt, uncertainty reduction is essential for UQ analysis informative. A large uncertainty in measured QoI confirms that the measurement is not informative. Park et al. [25] discuss the importance of uncertainty reduction in measured QoI for validation. The most dominant source of uncertainty in volume fraction measurement process is the uncertainty in the noisy calibration data. For noisy data, tradeoff between distributed fine sampling (exploration) and repetitive coarse sampling for a limited sampling budget is an interesting study for general uncertainty reduction. Matsumura et al. [26] report that distributed sampling often provides more accurate prediction than repetitive samples like the calibration samples. Since the samples are well distributed, adding more samples could reduce the uncertainty in the attenuation coefficient curve and so does the uncertainty in volume fraction.

4 The Effects of Epistemic Uncertainties on Measurements

In the Schlieren experiments, the measurement processing produced negligible sources of uncertainty, but the alignment introduced significant uncertainty. Figure 15(*a*) shows the front

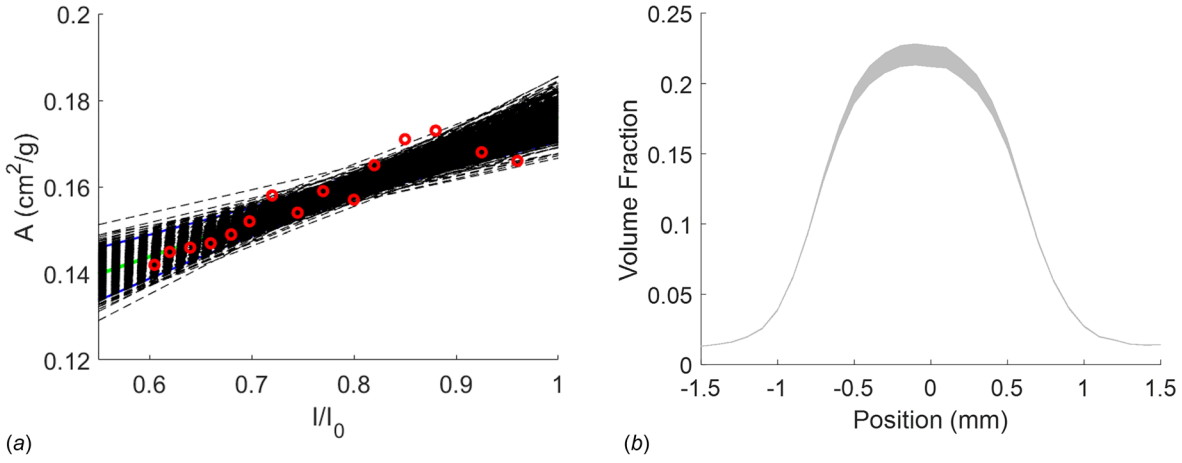

Fig. 13 The uncertainty in the estimation of the attenuation coefficient curve and its effect on a calculated volume fraction profile: (*a*) randomly generated possible attenuation coefficient curves and (*b*) uncertainty in particle volume fraction profiles ($t = 0$ μs) due to the uncertainty in the attenuation coefficient curve estimation

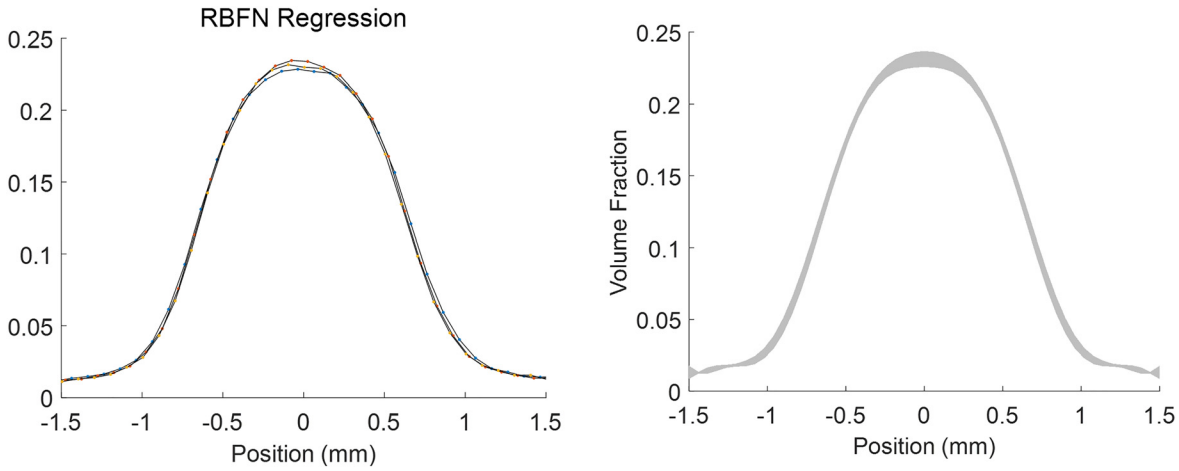

Fig. 14 X-ray volume fractions: (*a*) volume fraction profiles (three experiments) and (*b*) volume fraction with 95% confidence intervals

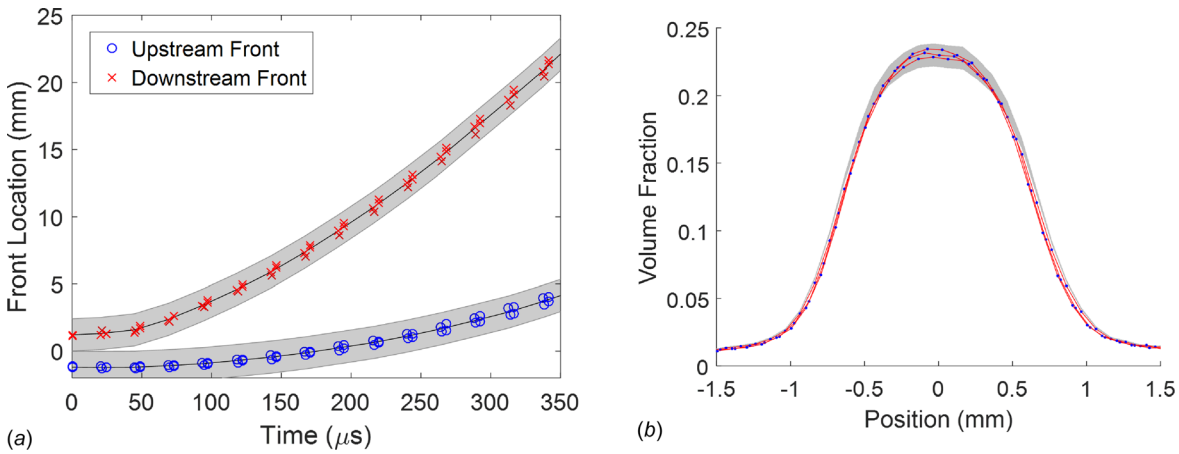

Fig. 15 Uncertainty in front locations and particle curtain volume fraction profiles: (*a*) epistemic uncertainty (gray band) and experimental variability (multiple circles) in curtain front locations and (*b*) computed uncertainty in particle volume fraction profile due to the uncertainty in the attenuation coefficient and the variability in the profiles ($t = 0\ \mu s$)

locations determined by the Schlieren image processing. The alignment uncertainty due to one-degree misalignment was applied to four experiments. The gray band shows the computed epistemic uncertainty of the four experiments. Front locations without considering the uncertainty are plotted with circles and crosses. The symbols (i.e., circles and crosses) form groups composed of four experiments at different times. Each group is not at the same time because of the timing uncertainty in taking the Schlieren images. The vertical difference between symbols of a group denotes the variability in the experiments. The experimental variability shown in the symbols is significantly lower than the epistemic uncertainty due to the alignment uncertainty. The epistemic uncertainty dominates the uncertainty in the front location measurements.

In the X-ray experiments, the uncertainty in the attenuation coefficient calibration was analyzed in this paper. Figure 15(*b*) shows the computed uncertainty in the volume fraction profiles from the uncertainty in the attenuation coefficient and the aleatory uncertainty estimated based on the three X-ray images. The gray bands are uncertainty profiles from the computed uncertainty using the double loop Monte Carlo Sampling. The lines are volume fraction calculations without considering the uncertainty in the calibration. In this case, the contribution of the computed uncertainty looks not significantly different from that of the epistemic uncertainty in the calculation but it is still larger than the variability estimated based on three experiments.

5 Conclusions

In this paper, we point out that in experiments measurements are often indirect, measuring one quantity and using a model to infer from it the desired quantity of interest. This leads to a necessity of quantifying the effect of epistemic uncertainty in the models on the measurements. Here, we perform this uncertainty quantification for a shock tube experiment with a shock hitting a curtain of glass particles. Both Schlieren and X-ray experimental measurements were used to infer particle front position and volume fraction distribution. Image processing, calibrating experiments, and experimental setup were studied. We found that the effects of epistemic uncertainties were much more significant than the variability on the uncertainty in the experimental measurements. This demonstrates the risk of using experimental measurements without quantifying epistemic uncertainties.

Quantifying epistemic uncertainty also identified significant uncertainty sources. For the front locations obtained using the Schlieren imaging technique, the alignment uncertainty in the light source was identified to be the largest uncertainty source. The dominant uncertainty in the volume fraction calculation based

on the X-ray imaging technique was the uncertainty in the attenuation curve estimation due to the uncertainty in the calibration test.

Funding Data

- This work was supported by the U.S. Department of Energy, National Nuclear Security Administration, Advanced Simulation and Computing Program, as a Cooperative Agreement under the Predictive Science Academic Alliance Program, under Contract No. DE-NA0002378 (Funder ID: 10.13039/100006168).

Nomenclature

A = X-ray attenuation coefficient
I = attenuated intensity of X-ray image
I_0 = reference intensity of X-ray image
φ_p = particle volume fraction

Appendix

The attenuation coefficient data were obtained from one continuous block. Thus, we assumed that the noise in the data is correlated. With the assumption, the observed attenuation coefficient $z(\mathbf{x})$ for intensity ratio $\mathbf{x}$ is modeled as

$$z(\mathbf{x}) = y(\mathbf{x}) + \varepsilon(\mathbf{x}) \tag{A1}$$

where $y(\mathbf{x})$ is the true trend and $\varepsilon(\mathbf{x})$ is the correlated noise model based on the GP [27,28]. In the GP model, the noise is modeled with a normal distribution $N(0, \sigma^2)$ at $\mathbf{x}$ and the spatial correlation between two different inputs is modeled with a multivariate normal distribution. The attenuation trend function is defined as

$$y(\mathbf{x}) = \mathbf{h}(\mathbf{x})^{\mathrm{T}}\boldsymbol{\beta} \tag{A2}$$

where $\mathbf{h}(\mathbf{x})$ is the basis function vector and $\boldsymbol{\beta}$ is the coefficient vector. For a one-dimensional linear trend function, the $\mathbf{h}$ vector is $\{1,\ x\}$. The correlation of noises between different inputs is defined with the Gaussian kernel as

$$r(\mathbf{x}, \mathbf{x}') = \prod_{k=1}^{m} \exp(-\theta_k (x_k - x_k')^2) \tag{A3}$$

where $(\mathbf{x}, \mathbf{x}')$ are two different points, m is the dimension of $\mathbf{x}$, and θ_i $(i = 1 \sim m)$ are hyperparameters of the correlation model to be estimated. The covariance of noises at two different inputs is defined based on the correlation function with process variance σ^2 as

$$\mathrm{Cov}(\varepsilon(\mathbf{x}), \varepsilon(\mathbf{x}')) = \sigma^2 r(\mathbf{x}, \mathbf{x}') \tag{A4}$$

Then, Eq. (A1) becomes a GP with a trend function of $y(\mathbf{x})$. The parameters $\boldsymbol{\theta}$, $\boldsymbol{\beta}$, and σ^2 should be estimated with data using a likelihood function with observed data $\mathbf{z}$ expressed as

$$L(\boldsymbol{\theta}, \boldsymbol{\beta}, \sigma^2 \,|\, \mathbf{z}) = \frac{1}{(2\pi)^{n/2}\sigma^n |\mathbf{R}|^{1/2}} \exp\left[-\frac{(\mathbf{z} - \mathbf{H}^{\mathrm{T}}\boldsymbol{\beta})^{\mathrm{T}} \mathbf{R}^{-1} (\mathbf{z} - \mathbf{H}^{\mathrm{T}}\boldsymbol{\beta})}{2\sigma^2} \right] \tag{A5}$$

where $\mathbf{H} = [\mathbf{h}(\mathbf{x}_1), \quad \ldots \quad, \mathbf{h}(\mathbf{x}_N)]^{\mathrm{T}}$ and $\mathbf{y} = [y_1 \quad \ldots \quad y_N]^{\mathrm{T}}$. $\mathbf{R}$ is N by N matrix and its (i, j) component is defined with $r(\mathbf{x}_i, \mathbf{x}_j)$. The maximum likelihood estimators of $\boldsymbol{\beta}$, σ^2 can be analytically derived as a function of $\boldsymbol{\theta}$. The maximum likelihood estimators are obtained as

$$\hat{\boldsymbol{\beta}} = (\mathbf{H}^{\mathrm{T}}\mathbf{R}^{-1}\mathbf{H})^{-1}\mathbf{H}^{\mathrm{T}}\mathbf{R}^{-1}\mathbf{z} \tag{A6}$$

$$\hat{\sigma}^2 = \frac{(\mathbf{z} - \mathbf{H}\hat{\boldsymbol{\beta}})^{\mathrm{T}} \mathbf{R}^{-1} (\mathbf{z} - \mathbf{H}\hat{\boldsymbol{\beta}})}{N} \tag{A7}$$

where the "hat" denotes a maximum likelihood estimator. By substituting Eqs. (A6) and (A7) into (A5), the likelihood function is reformulated as

$$L\left(\theta \,|\, \hat{\beta}, \hat{\sigma}^2, \mathbf{z}\right) \propto \frac{1}{\hat{\sigma}^n |\mathbf{R}|^{1/2}} \tag{A8}$$

By subscripting the estimated parameters to the GP model, possible attenuation coefficient curves can be generated using Eq. (A1). A curve values at $\mathbf{x}_{\mathrm{test}}$ follow a multivariate normal distribution as

$$z(\mathbf{x}_{\mathrm{test}}) \sim N(\mathbf{h}(\mathbf{x}_{\mathrm{test}})^{\mathrm{T}}\boldsymbol{\beta}, \mathbf{R}_{\mathrm{test}}) \tag{A9}$$

Note that the observed data $z(\mathbf{x}_{\mathrm{test}})$ follow a normal distribution at the test point but it is correlated with an observed data at a different test point.

References

[1] Oberkampf, W. L., and Trucano, T. G., 2002, "Verification and Validation in Computational Fluid Dynamics," Prog. Aerosp. Sci., **38**(3), pp. 209–272.
[2] Trucano, T. G., Swiler, L. P., Igusa, T., Oberkampf, W. L., and Pilch, M., 2006, "Calibration, Validation, and Sensitivity Analysis: What's What," Reliab. Eng. Syst. Saf., **91**(10–11), pp. 1331–1357.
[3] Schwer, L. E., 2006, "Guide for Verification and Validation in Computational Solid Mechanics," American Society of Mechanical Engineering, New York, Standard No. PTC 60/V&V 10.
[4] Oberkampf, W. L., Trucano, T. G., and Hirsch, C., 2004, "Verification, Validation, and Predictive Capability in Computational Engineering and Physics," ASME Appl. Mech. Rev., **57**(5), pp. 345–384.
[5] Roy, C. J., and Oberkampf, W. L., 2011, "A Comprehensive Framework for Verification, Validation, and Uncertainty Quantification in Scientific Computing," Comput. Methods Appl. Mech. Eng., **200**(25–28), pp. 2131–2144.
[6] Oberkampf, W. L., and Barone, M. F., 2006, "Measures of Agreement Between Computation and Experiment: Validation Metrics," J. Comput. Phys., **217**(1), pp. 5–36.
[7] Li, W., Chen, W., Jiang, Z., Lu, Z., and Liu, Y., 2014, "New Validation Metrics for Models With Multiple Correlated Responses," Reliab. Eng. Syst. Saf., **127**, pp. 1–11.
[8] Ferson, S., Kreinovich, V., Hajagos, J., Oberkampf, W., and Ginzburg, L., 2007, "Experimental Uncertainty Estimation and Statistics for Data Having Interval Uncertainty," Sandia National Laboratories, Albuquerque, NM, Report No. SAND2007-0939.
[9] Beresh, S. J., 2008, "Evaluation of PIV Uncertainties Using Multiple Configurations and Processing Techniques," AIAA Paper No. 2008-0239.
[10] Hughes, K. T., Diggs, A., Park, C., Littrell, D., Haftka, R. T., Kim, N. H., and Balachandar, S., 2018, "Simulation-Driven Experiments of Macroscale Explosive Dispersal of Particles," AIAA Paper No. 2018-1545.
[11] Thurber, M. C., 1999, "Acetone Laser-Induced Fluorescence for Temperature and Multiparameter Imaging in Gaseous Flows," Ph.D. thesis, Stanford University, Stanford, CA, p. 137.
[12] Adrian, R. J., and Westerweel, J., 2011, "Particle Image Velocimetry (No. 30)," Cambridge University Press, Cambridge, UK.
[13] Timmins, B. H., Wilson, B. W., Smith, B. L., and Vlachos, P. P., 2012, "A Method for Automatic Estimation of Instantaneous Local Uncertainty in Particle Image Velocimetry Measurements," Exp. Fluids, **53**(4), pp. 1133–1147.
[14] Hughes, K., Park, C., Haftka, R., and Kim, N. H., 2017, "Forensic Uncertainty Quantification of Explosive Dispersal of Particles," AIP Conference Proceedings 1979, St. Louis, MI, July 9–14, p. 140001.
[15] Ling, Y., Wagner, J. L., Beresh, S. J., Kearney, S. P., and Balachandar, S., 2012, "Interaction of a Planar Shock Wave With a Dense Particle Curtain: Modeling and Experiments," Phys. Fluids, **24**(11), p. 113301.
[16] Wagner, J. L., Beresh, S. J., Kearney, S. P., Trott, W. M., Castaneda, J. N., Pruett, B. O., and Baer, M. R., 2012, "A Multiphase Shock Tube for Shock Wave Interactions With Dense Particle Fields," Exp. Fluids, **52**(6), pp. 1507–1517.
[17] Wagner, J. L., Beresh, S. J., Kearney, S. P., Pruett, B. O., and Wright, E. K., 2012, "Shock Tube Investigation of Quasi-Steady Drag in Shock-Particle Interactions," Phys. Fluids, **24**(12), p. 123301.
[18] DeMauro, E. P., Wagner, J. L., Beresh, S. J., and Farias, P. A., 2017, "Unsteady Drag Following Shock Wave Impingement on a Particle Curtain Measured Using Pulse-Burst PIV," Phys. Rev. Fluids, **2**(6), p. 064301.
[19] Parmar, M., Haselbacher, A., and Balachandar, S., 2009, "Modeling of the Unsteady Force in Shock-Particle Interaction," Shock Waves, **19**(4), pp. 317–329.
[20] Park, C., Fernández-Godino, M. G., Kim, N. H., and Haftka, R. T., 2016, "Validation, Uncertainty Quantification and Uncertainty Reduction for a Shock Tube Simulation," AIAA Paper No. 2016-1192.

[21] Wagner, J. L., Kearney, S. P., Beresh, S. J., DeMauro, E. P., and Pruett, B. O., 2015, "Flash X-Ray Measurements on the Shock-Induced Dispersal of a Dense Particle Curtain," Exp. Fluids, **52**(12), p. 213.
[22] Linne, M., 2013, "Imaging in the Optically Dense Regions of a Spray: A Review of Developing Techniques," Prog. Energy Combust. Sci., **39**(5), pp. 403–440.
[23] Busch, K. W., and Busch, M. A., 1999, "Introduction to Cavity-Ringdown Spectroscopy," *Cavity-Ringdown Spectroscopy—An Ultratrace-Absorption Measurement Technique*, K. W. Busch, and M. A. Busch, eds., ACS Publications, Washington, DC, pp. 7–19.
[24] MacPhee, A. G., Tate, M. W., Powell, C. F., Yue, Y., Renzi, M. J., Ercan, A., Narayanan, S., Fontes, E., Walther, J., Schaller, J., and Wang, J., 2002, "X-Ray Imaging of Shock Waves Generated by High-Pressure Fuel Sprays," Science, **295**(5558), pp. 1261–1263.
[25] Park, C., Nili, S., Mathew, J. T., Kim, N. H., and Haftka, R. T., 2018, "Uncertainty Investigation for Shock Tube Simulation Error Quantification," AIAA Paper No. 2018-1662.
[26] Matsumura, T., Haftka, R. T., and Kim, N. H., 2015, "Accurate Predictions From Noisy Data: Replication Versus Exploration With Applications to Structural Failure," Struct. Multidiscip. Optim., **51**(1), pp. 23–40.
[27] Kennedy, M. C., and O'Hagan, A., 2001, "Bayesian Calibration of Computer Models," J. R. Stat. Soc.: Ser. B, Stat. Methodol., **63**(3), pp. 425–464.
[28] Rasmussen, C. E., 2004, "Gaussian Processes in Machine Learning," *Advanced Lectures on Machine Learning*, Springer, Berlin, pp. 63–71.